Polymer 311 (2024) 127523

Contents lists available at ScienceDirect

Polymer

journal homepage: www.elsevier.com/locate/polymer

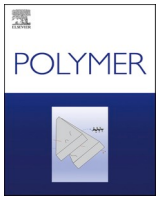

Advanced 3D printed bone scaffolds with sodium alginate/Tri-calcium phosphate/probiotic bacterial hydroxyapatite: Enhanced mechanical and biocompatible properties for bone tissue engineering

Sabereh Nouri [a,b], Giti Emtiazi [a], Songul Ulag [b,c], Oguzhan Gunduz [b,c,*], Ayse Ceren Calikoglu Koyuncu [b,c], Rasoul Roghanian [a], Armaghan Moradi [b,c], Rasoul Shafiei [a], Ari Tukay [d], Hilal Turkoglu Sasmazel [d]

[a] Department of Cell and Molecular Biology and Microbiology, Faculty of Biological Science and Technology, University of Isfahan, Isfahan, Iran
[b] Center for Nanotechnology & Biomaterials Application and Research (NBUAM), Marmara University, Istanbul, Turkey
[c] Faculty of Technology, Marmara University, Department of Metallurgical and Materials Engineering, Istanbul, Turkey
[d] Metallurgical and Materials Engineering Department, Faculty of Engineering, Atilim University, Incek, Ankara, Turkey

ARTICLE INFO

Keywords:
Bone scaffold
3D printing
Probiotic bacterial hydroxyapatite
Biocompatibility

ABSTRACT

Introduction: The increasing prevalence of severe bone diseases, such as osteoporosis and critical bone defects, necessitates the development of more effective bone substitutes. This study addresses this need by investigating 3D-printed bone scaffolds composed of sodium alginate and tricalcium phosphate, enhanced with three distinct types of hydroxyapatite (HA): bovine-derived HA, commercially available HA, and HA enriched with probiotic bacteria. We aim to evaluate the performance of these scaffolds in terms of mechanical strength, biocompatibility, and their ability to support bone regeneration.

Methods: The scaffolds were analyzed through various tests, including X-ray Diffraction (XRD), Fourier Transform Infrared Spectroscopy (FTIR), Differential Scanning Calorimetry (DSC) to characterization. Scanning Electron Microscopy (SEM) was used to examine pore structure, while swelling and degradation tests evaluated the scaffold's stability. Compression testing determined mechanical strength, and in vitro cell culture assays assessed cell proliferation, osteogenic differentiation, and biomineralization.

Results: SEM results indicated that 3D scaffolds with probiotic bacterial HA had the desired 472 μm pore size. These scaffolds demonstrated a strain of 29.26 % and a compressive strength of 10 MPa, meeting the mechanical standards of human trabecular bone. Cell culture studies revealed enhanced cell proliferation by 50 %, osteogenic differentiation with 15.3 U/mg ALP activity, and 1.22-fold biomineralization, suggesting they are highly biocompatible and promote bone growth.

Conclusion: Probiotic bacterial HA scaffolds exhibit ideal properties and biocompatibility, enhancing bone regeneration and serving as an ideal alternative to chemical types.

1. Introduction

Bones make up about 15 % of body weight and are the largest structural system, providing skeleton support, enabling motor functions, producing blood cells, and protecting organs [1]. Bone defects from tumors, infections, trauma, and disorders impose significant health and economic burdens. Bone transplantation is a common solution, with options including biological grafts (autografts and allografts) and non-biodegradable implants (metallic and ceramic) [2]. However, these methods have drawbacks, including limited availability and potential post-surgical complications. Regenerative medicine aims to repair tissues using biodegradable 3D scaffolds, cells, and growth factors. Effective scaffolds require intricate designs with specific internal structures, porosity, and bioactivity. Creating these products involves innovative

* Corresponding author. Center for Nanotechnology & Biomaterials Application and Research (NBUAM), Marmara University, Istanbul, Turkey.
E-mail addresses: Sabere.nuri@yahoo.com (S. Nouri), emtiazi@sci.ui.ac.ir (G. Emtiazi), songul.ulag@marmara.edu.tr (S. Ulag), oguzhan@marmara.edu.tr, ucemogu@ucl.ac.uk (O. Gunduz), aceren@marmara.edu.tr (A.C. Calikoglu Koyuncu), r.roghanian@sci.ui.ac.ir (R. Roghanian), armaghan.moradi@gmail.com (A. Moradi), r.shafiei@sci.ui.ac.ir (R. Shafiei), tukayari@yahoo.fi (A. Tukay), hilal.sasmazel@atilim.edu.tr (H.T. Sasmazel).

https://doi.org/10.1016/j.polymer.2024.127523
Received 27 April 2024; Received in revised form 10 August 2024; Accepted 20 August 2024
Available online 24 August 2024

techniques due to their complex compositions and sensitivity to manufacturing conditions [3]. Replicating the composition, structure, and mechanical properties of human tissues is crucial in developing biomaterials for tissue engineering scaffolds, which must support cell growth and proliferation. Effective scaffold design for bone tissue engineering involves ensuring oxygen and nutrient transport, removing cell metabolites, and promoting cell attachment. Successful bone repair requires addressing tissue regeneration, antibacterial properties, and scaffold customization. 3D printing, with its layer-by-layer technique, is ideal for creating complex, porous scaffolds that mimic bone tissue. Notable clinical applications include porous titanium implants and other 3D-printed scaffolds [4,5].

In the quest to develop effective tissue engineering scaffolds, incorporating materials that closely mimic biological frameworks is crucial. Research indicates that sodium alginate (SA) is particularly effective in stabilizing matrix scaffolds and guiding cell growth due to its excellent biocompatibility and gelation properties. However, while SA is well-regarded in biomedical material engineering, using it as a sole component in 3D printing bioinks presents challenges and often fails to meet clinical requirements. To overcome these limitations, incorporating inorganic materials with SA can enhance the mechanical properties of scaffolds and promote better bone regeneration [6]. SA is a biopolymer typically derived from brown seaweed, composed of β-D-mannuronic acid and α-L-guluronic acid residues. Depending on its source and processing methods, its structure can vary from semi-crystalline to amorphous. X-ray diffraction (XRD) studies often show sodium alginate as primarily amorphous especially in its hydrated or gel form sometimes with some crystalline regions, particularly in dried forms or when interacting with certain additives [7].

Bioceramics are used in biomedical applications for their biocompatibility and mechanical properties. Notable biodegradable types include porous calcium phosphate, calcium sulfate, bioactive glasses and calcium silicate. Porous calcium phosphate mimics bone minerals, aiding bone regeneration by releasing calcium and phosphate ions [8]. Hydroxyapatite (HA) is a crucial inorganic component of human bones, extensively used in bone tissue repair due to its biocompatibility and osteoinductive properties. HA forms chemical bonds with tissues and is partially soluble in the body. Metabolic ions released from calcium phosphate-based implants are non-toxic and promote bone tissue defect healing by participating in calcium and phosphorus metabolism [4].

Various chemical methods synthesize HA [9,10]. These processes often use chemicals for controlled synthesis, but resulting HA from chemical approaches can sometimes be toxic due to their morphology [10,11]. Recently, green synthesis has gained interest for its eco-friendly, cost-effective, and easy-to-implement nature. Green synthesis refers to the use of biological sources and approaches to achieve materials, leveraging natural processes and organisms to produce substances in an environmentally sustainable manner. Modern nano-biotechnology focuses on creating nanomaterials in an environmentally friendly way, with microorganisms having significant potential to produce these nanomaterials through biological processes [12]. is derived from green sources like animal bone tissue, poultry, fish, coral, shrimp shells, snakeskin, hedgehog thorns, plants, fungi, and algae [1,9,13].

Bacteria-mediated biomineralization is a green approach to synthesizing nano-HA, offering advantages over other methods. However, its applications are under-researched [11,13]. Bacteria can serve as bio-manufacturers for nano-synthesis through biomineralization, producing inorganic crystals with controlled morphology and nanostructure [14]. Biomineralization allows biological processes to dictate the shape, phase, orientation, and nanostructure of inorganic crystals [13]. Probiotics offer cost-effective, environmentally friendly solutions in medicine, food, and pharmaceuticals. Developing probiotic bacterial biosynthesis methods involves considering large-scale production feasibility, probiotic bacterium safety, and human health significance [14]. The production of biological nano-HA through probiotic bacteria has the potential to offer a novel, non-toxic, and biocompatible composite suitable for diverse applications in biomedicine, food additives, and environmental contexts. Prior research has indicated that this particular form of probiotic bacterial HA can induce the differentiation of stem cells from human-exfoliated deciduous teeth into osteoblastic cells, fostering the proliferation of osteoblast cell lines [14,15].

This study successfully fabricated bone scaffolds using 3D printing technology with various types of HA, including commercial HA, bovine HA, and probiotic bacterial nano-HA. To assess the scaffolds, we employed key testing methods: comprehensive characterization included X-ray Diffraction (XRD) for structural analysis, Fourier Transform Infrared Spectroscopy (FTIR) and Differential Scanning Calorimetry (DSC) for compositional and thermal properties, and Scanning Electron Microscopy (SEM) for microstructural evaluation. Additional tests included swelling and degradation assessments, compression testing for mechanical strength, and in vitro cell culture assays to evaluate cell proliferation, osteogenic differentiation, and biomineralization. The hypothesis posits that HA scaffolds derived from probiotic bacteria would exhibit superior properties, making them ideal for biomedical applications. To our knowledge, this study is the first to demonstrate the superior performance of probiotic bacterial HA scaffolds compared to bovine and commercial counterparts.

2. Materials and methods

2.1. Materials

The components of the Pikovskaya medium (PVK) used in this study included nutrient agar, dextrose, $Ca_3(PO_4)_2$, NaCl, KCl, $MgSO_4{\cdot}7H_2O$, yeast extract, $FeSO_4{\cdot}7H_2O$, $MnSO_4{\cdot}H_2O$, and agar-agar, all sourced from Merck, Germany. Additional materials included sodium alginate, DMEM/F-12, fetal bovine serum, penicillin, streptomycin, L-glutamine, DMSO, tetrazolium, 5-Bromo-4-Chloro-3-Indolyl phosphate, alizarin red stain, and 3-(4,5-dimethylthiazol-2-yl)-2,5-diphenyl-2H-tetrazolium bromide, obtained from Sigma-Aldrich, USA. Commercial hydroxyapatite (CHA) was supplied by Oerlikon Metco, Switzerland, while beta-tricalcium phosphate (TCP) and calcium chloride ($CaCl_2$) were procured from Merck, Germany. Phosphate-buffered saline was obtained from Gibco, USA. Bovine-derived hydroxyapatite (Bovine-HA) was provided by the Center of Nanotechnology & Biomaterials Application and Research (NBUAM) at Marmara University.

2.2. Bacterial HA synthesis

The standard probiotic strain *Bacillus coagulans* (ATCC 7050) was cultured using a streak plate method on a PVK medium, which was supplemented with urea. After inoculation, the plates were incubated at 37 °C for five days to allow the bacteria to grow and form spread colonies all over the plate. Following the incubation period, the bacterial cultures were carefully harvested. The harvested bacterial biomass was then subjected to air-drying at room temperature (25 °C) with a relative humidity of 18 % for 24 h. This drying step ensures that excess moisture is removed. After drying, the bacterial mass underwent a purification process. This was achieved by heating the dried bacteria in a laboratory furnace (Nabertherm, Germany) at a temperature of 600 °C for 2 h. This high-temperature treatment effectively kills any residual bacteria and induces the formation of purified HA from the bacterial biomass. The result of this process is purified HA derived from the probiotic bacteria, which is now ready for use in various applications [14].

2.3. Solutions preparation and characterization

The solutions used in the construction of scaffolds were prepared according to the following details. Initially, three separate solutions, each containing 0.8 g SA, were dissolved in 10 ml of distilled water at 37 °C for 15 min with continuous stirring at a constant temperature

using a magnetic stirrer. Subsequently, 4 g TCP was introduced into the solutions and thoroughly blended. Afterward, 4 g of bovine-derived HA (BHA), commercial HA (CHA), and probiotic bacterial HA (PHA) were individually incorporated into each of the three solutions. Beta-tricalcium phosphate promotes a modest regeneration of bone tissue by stimulating cells. It facilitates interaction between osteoblastic and osteoclastic cells and has a porous structure similar to trabecular bone, which enhances vascularization and osteogenesis. This leads to cell migration and proliferation, though it has low mechanical strength. Conversely, hydroxyapatite is highly osteoconductive and resorbs slowly due to its high calcium and phosphate content, providing it with high load-bearing strength. To control and check various parameters with different types of hydroxyapatites, we used beta-tricalcium phosphate as a consistent substrate. Viscosity, indicating the rheological properties of the composite scaffold solutions, was measured using a digital viscometer (RM 200 CP 4000 Plus, Lamy Rheology, France). Prior to conducting the tests, the apparatus underwent calibration, and each sample was tested in triplicate under conditions of a shear rate of 60 s^{-1} and a room temperature of 25 °C.

2.4. Design and scaffolds 3D printing

A scaffold model measuring 5 × 5 × 3 mm^3 was created using SolidWorks, a versatile software that encompasses CAD, CAE, and CAM functions. Subsequently, this design was converted to G-code using Simplify programming which enables users to programmatically control various process settings, serving as the interface for the 3D printer, where all adjustments and configurations pertinent to the printing process can be made. The G-code for the scaffold design was then transferred to RepetierHost software for printing using a 3D bioprinter (AXO-A3, Axolotl Biosystems, Turkey). A 22g needle with a diameter of 0.41 mm was immediately connected to a 10 mL Luer lock syringe containing the solutions (at a room temperature of 25 °C). Uniform parameters, including a contact angle of 90° and a fill density of 40 %, were applied to all the samples. The optimal bioprinting conditions were achieved at a printing speed of 4 mm/s. Each scaffold consisted of a total of 8 layers (Figure SI1). Figures SI2 illustrating the printing process and photographs of the printed samples.

2.5. Crosslinking process

To initiate the cross-linking process, the printed scaffolds were immersed in a 5 % calcium chloride solution after the scaffolds were 3D printed. Room temperature was maintained throughout this procedure for 24 h to ensure complete cross-linking. Following this, the scaffolds underwent a freezing step at −50 °C for 2 h. Finally, the cross-linked porous scaffolds were subjected to freeze-drying for 24 h (Alpha 1–2 LD Plus Freeze-dryer, Chirist, Germany). The lyophilization process resulted in the evaporation of a significant volume of water from within the scaffold, creating numerous voids in the interior of the printed scaffolds [4].

2.6. Scaffold characterization

2.6.1. Morphology and phase composition characterization

2.6.1.1. Scanning electron microscopy (SEM). SEM images of the 3D-printed samples were meticulously obtained using a scanning electron microscope (EVO MA10, Zeiss, Germany). The microscope operated at an acceleration voltage of 10 kV, chosen for optimal resolution of the sample details. Before imaging, a thin, uniform coating of palladium and gold was applied to the samples using a sputter coater (SC7620, Quarum, USA). This coating, conducted at 3 kV for precisely 60 s, was essential to impart electrical conductivity to the surfaces. Such conductivity ensured the acquisition of high-quality SEM images, facilitating detailed morphological observations necessary for thorough analysis [16].

2.6.1.2. X-ray diffraction (XRD). The phase composition of the scaffold was analyzed using XRD with CuKα radiation (XRD-6100 LabX, Shimadzu, Japan). The XRD instrument operated at a current of 30 mA and a voltage of 40 kV. Scanning was performed in the 2θ range of 10°–90° at a scanning rate of 2° per minute. The obtained data were analyzed using software (OriginPro 7.0, OriginLab Corporation, USA) [17].

2.6.2. Chemical and thermal analysis of the scaffolds

2.6.2.1. Fourier transform-infrared spectroscopy (FT-IR). The molecular structure and chemical composition of the scaffolds were assessed using FTIR (FT-IR-4700, JASCO, Japan). Transmittance was measured within the wavenumber range of 4000 to 400 cm^{-1}. Attenuated total reflection (ATR) was employed for more accurate peak measurements, with each test comprising 18 scans [18].

2.6.2.2. Differential scanning calorimetry (DSC). A differential scanning calorimeter was used to measure the 3D bio-printed scaffolds' thermal characteristics (DSC-60 Plus, Shimadzu, China). The tests were conducted with a scanning rate of 10 °C per minute in the 20–400 °C temperature range [19,20].

2.6.3. Wettability

2.6.3.1. In vitro swelling test. The swelling characteristics of the composite scaffolds were examined over 14 days using phosphate-buffered saline (PBS) and a thermo-shaker (TS-100C, Biosan, Latvia) operating at 37 °C and 250 rpm. The swelling test was performed on three samples per scaffold. At the beginning of each experiment, the dry scaffolds were gravimetrically weighed to establish their initial weight (Wi). Subsequently, they were immersed in Eppendorf tubes containing PBS with a pH of 7.4. Before each wet weight measurement (Ww) was conducted every 24 h, the composite scaffolds were gently cleaned using filter paper to remove any residual saline from the surface. For the next measurement, stale PBS was used again for the solution at each interval.

Swelling rate (S) was calculated based on the dry weight using Equation (1) [21].

$$S = \frac{(Ww - Wi)}{Wi} \times 100 \quad (1)$$

Wi: initial weight, Ww: wet weight.

2.6.3.2. In vitro degradation test. In vitro biodegradation studies were carried out in test tubes filled with a phosphate-buffered saline (PBS) solution (pH 7.4), followed by incubation. The initial weights (Wi) of the scaffolds were determined before the commencement of the studies. Subsequently, the scaffolds were gently placed in PBS-filled containers and incubated in an oven set at 37 °C. After 24 h, the scaffolds were left in the oven (37 °C) to air-dry for an additional 24 h, ensuring complete drainage of PBS from the Eppendorf tube. The thoroughly dried weight (Wd) was then measured. The measured scaffolds were then placed in fresh PBS for the next measurement, and the process was repeated for up to 15 days. Wi represents the sample weight before immersion in PBS, and Wd represents the sample weight after the degradation test, determined after the drying process.

Equation (2) was used to calculate the extent of degradation [21].

$$S = \frac{(Wi - Wd)}{Wi} \times 100 \quad (2)$$

Wi: initial weight, Wd: dried weight.

2.6.4. Mechanical properties

Firstly, the compression testing equipment used (EZ-LX, Shimadzu Corporation, Japan), which allows for precise control over compression parameters. The compression rate was set at 1 mm/min to ensure consistency across all tests. Additionally, the compression testing was conducted in accordance with ASTM C1424-15 (Standard Test Method for Monotonic Compressive Strength of Advanced Ceramics at Ambient Temperature 2019) to ensure consistency and comparability in the experimental results. Prior to mechanical testing, all scaffolds underwent thorough drying under controlled conditions to minimize moisture content variability. Controlled conditions were the drying process involved placing the scaffolds in a freeze-dryer for 24 h until a constant weight was achieved. Furthermore, the test specimens were prepared with uniform dimensions to eliminate any potential sources of variability [22–24]. The gauge length, thickness, and breadth of each test specimen were precisely controlled at 2.2 mm, 7 mm, and 7 mm, respectively.

2.7. Cell culture studies

Using the MC3T3-E1 mouse osteoblast cell line (provided by the Department of Bioengineering at Kirikkale University), cell culture investigations were conducted to biologically characterize 3D printed scaffolds containing bovine HA, bacterial HA, and commercial HA. All scaffolds comprised 40 % TCP and 40 % HA. After being shaped into cylinders, the 3D printed scaffolds underwent UV light exposure for 45 min for sterilization. The specimens were arranged in 24-well plates, and MC3T3-E1 cells were cultured for 21 days at 37 °C with 5 % CO_2 at a seeding rate of 2×10^4 cells/mL on the prepared scaffolds. The culture medium included 1 % v/v penicillin-streptomycin, 1 % v/v L-glutamine, DMEM/F-12, and 10 % v/v FBS. Alizarin Red Staining was employed to identify calcium deposition, the MTT Assay assessed cell viability, and alkaline phosphatase (ALP) Activity evaluated differentiation. Each test was completed over 21 days. Tissue culture polystyrene (TCPS) served as the control for every experiment. Exponentially growing cells were plated in flat 24-well plates (Corning, USA) at a density of 5×10^4 cells per well. The seeded culture medium, mimicking TCPS conditions, included 10 % (v/v) FBS. Subsequently, culture media were added in a series of progressively diluted concentrations to achieve a final volume of 2 mL per well [25].

2.7.1. MTT assay

On days 1, 7, 14, and 21, the viability of MC3T3-E1 osteoblast cells on 3D printed materials was assessed using the MTT test. After the 37 °C and 5 % CO_2 incubation, the cell culture medium was withdrawn, and all specimens were thoroughly washed with PBS. Subsequently, 900 μL of fresh medium and 100 μL of MTT solution were added to each well after the washing process. The samples were then incubated for an additional 3 h. Following this, formazan crystals formed during the incubation were dissolved in 2 ml of DMSO, and the solution was incubated again, with subsequent removal of the MTT solution. Finally, the medium was aspirated from the wells, and a microplate reader (LEDETECT96, Dynamica, Switzerland) was utilized to measure the absorbance values of the solution at 540 nm [26].

2.7.2. ALP activity

On days 7, 14, and 21 of the cultivation, the ALP activity of the cultured 3D-printed scaffolds was assessed. To create the substrate solution, 10 ml of distilled water (DW) was used to dissolve a tablet containing nitro blue tetrazolium and 5-Bromo-4-Chloro-3-Indolyl Phosphate (NBT/BCIP). After preparation, the substrate solution was kept at 25 °C for 2 h in the dark. Following the removal of the cultivated samples from the incubator and gentle disposal of the media, the cells underwent three rounds of PBS washing. Subsequently, samples were immersed in 10 % formalin solution and allowed to stand for a maximum of 60 s. Following the elimination of the formalin solution, the samples underwent three PBS washes. After adding the substrate solution and a 10 min incubation period at 25 °C, measurements were taken at 405 nm[15, 27, 28].

2.7.3. Alizarin red staining

Calcium accumulation in the cell-seeded scaffolds was visualized through alizarin red staining. To prepare the stain, 2 g of alizarin red was dissolved in 10 mL of DW, and the pH of the mixture was carefully adjusted to 4 using HCl. The resulting solution was kept in the dark until needed. After pre-incubation of the scaffolds with cells, they were washed with PBS. To fix the cells, 10 % formalin was applied to the wells and left for 30 min. Following the removal of formalin, cells were washed with DW, and a dye solution was applied to the samples. The samples were then left to incubate at 25 °C for half an hour in the dark. Subsequently, the samples underwent centrifugation at 900*g*. Finally, the amount of calcium deposition was determined by measuring the absorbance values of the respective solutions at 405 nm using a microplate reader [27,28].

2.8. Statistical analysis

The data were collected using descriptive statistics, and the results were visually presented through graphical representations. Statistical analysis was performed using Prism, a software application developed by software (GraphPad Inc, USA). One-way and two-way ANOVA were employed to assess mean differences among groups. Following significant ANOVA results, Tukey's multiple comparison tests were applied as post hoc analysis to determine specific group differences. A significance threshold of $^*P < 0.05$ was set for statistical significance.

3. Results and discussion

3.1. Physical characterizations of the solutions

The characteristics of the solution can play a substantial role and may impose constraints, as they directly impact the quality of the end product. Viscosity is a critical factor to consider in ensuring the success of the 3D printing process. To maintain their form during printing and crosslinking, polymer solutions must possess sufficient viscosity. Research findings indicate that reduced viscosity is known to improve cell adherence, but it can also make 3D-printed objects unstable. It is important to note that the solution's viscosity must strike a balance. While maintaining a low enough profile to facilitate seamless printing, it must be robust enough to sustain the layer-by-layer building process. Furthermore, it has been shown that pore connections may be impacted by the solution's viscosity [29,30]. The analysis of viscosity measurements for various solutions is provided below. The BHA solution exhibited the lowest viscosity, measuring at 486,000 mPa s, followed by the CHA solution with a viscosity of 502,000 mPa s, and the PHA solution had the highest viscosity, reaching 522,000 mPa s. Previous research has suggested that increased viscosity can result in irregular scaffold structures and printing challenges in 3D bioprinting. Given that printability is influenced by various factors, the viscosity of the solution emerges as a critical parameter in the 3D printing process. A solution with elevated viscosity may lead to needle tip clogging, hindering the printing of subsequent layers. Conversely, insufficient viscosity can cause printed strands to spread, causing adjacent layers to merge and subsequent layers to collapse. Therefore, it is essential to carefully adjust and select the viscosity of solutions for optimal 3D printing outcomes. In the case of the viscosity feature, this study observed that the viscosity increase, up to 522,000 mPa s, had no adverse effects on 3D printer printability and enabled the performance of characterization tests on the composite structures [21].

3.2. Scaffolds characterization

3.2.1. Morphological and phase composition characterization

3.2.1.1. SEM imaging and pore size analysis. The surface morphologies of the 3D-printed scaffolds were examined using SEM. As depicted in Fig. 1, all scaffolds exhibited uniformly distributed pores, and the integrity of the scaffold was effectively maintained irrespective of the source of HA. The BHA scaffold, in particular, displayed pores that were more rounded and smaller compared to the other scaffolds. The difference is likely due to the lower viscosity of the BHA solution. This low viscosity caused printed leyers to spread during fabrication, resulting in smaller and more rounded pores compared to the standard cubic pores in PHA scaffolds. Both CHA and PHA showed similar surface structures and pore sizes, with PHA presenting a more regular distribution of pores. To determine the average pore size, the diameters of 24 pores were measured using Image J. The mean pore sizes were within a comparable range for BHA (405.16 ± 23.52 μm), CHA (507.75 ± 26.65 μm), and PHA (472.17 ± 18.51 μm). In the field of bone tissue engineering, it is well-established that cellular growth and bone ingrowth are facilitated within a range of pore sizes typically falling between 100 and 1000 μm. It can be affirmed that the manufactured scaffolds possess an appropriate spectrum of pore sizes conducive to supporting cellular growth and bone ingrowth in applications related to bone tissue engineering [16]. In previous findings by the authors, the elemental composition and Ca/P ratios of samples were determined using EDX analysis. The Ca/P ratio of synthesized nanoparticles from *Bacillus coagulans* was found to be 2.7. The higher ratio in the biosynthesized nano-HA, compared to the standard HA ratio of 1.8, is likely due to the presence of calcite and decomposed calcite from heat-treated samples. Calcite is recognized as a bio-ceramic involved in osteogenesis, with numerous applications in medicine and orthopedics. After purification, the Ca/P ratio of the synthesized HA was reduced to 1.8. XRF analysis was employed to perform quantitative chemical analysis of the biosynthesized material elements. The primary components of HA were calcium and phosphorus, with minor amounts of other elements. The purification of HA was confirmed by XRF. Additionally, the synthesized nanoparticles contained trace amounts of other elements such as silicon, magnesium, sodium, potassium, zinc, and other elements likely utilized by the bacteria from the culture medium [14].

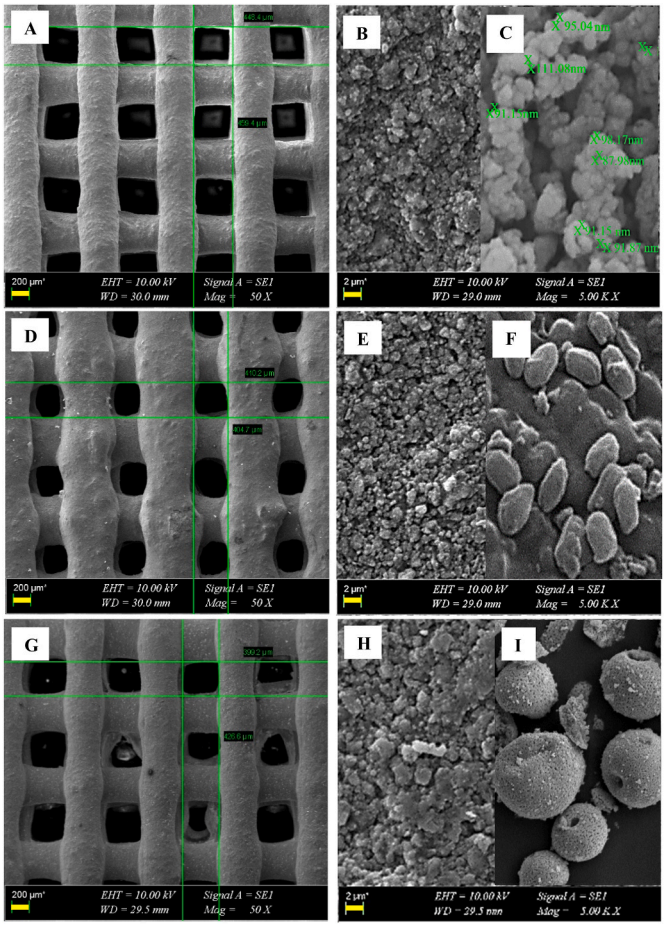

Fig. 1. SEM images of crosslinked scaffolds at 50x and 5000× magnifications, captured with an accelerating voltage of 10.00 kV. (A) PHA scaffolds at low magnification, showing pore sizes of ~472 μm; (B) high magnification detailing the surface morphology; (C) probiotic-mediated hydroxyapatite at a 2 μm scale. (D) BHA scaffolds at low magnification, with pore sizes of ~405 μm; (E) high magnification detailing surface morphology; (F) bovine-mediated hydroxyapatite at a 2 μm scale. (G) CHA scaffolds at low magnification, displaying pore sizes of ~392.2 μm and 426.6 μm; (H) high magnification detailing surface morphology; (I) commercial hydroxyapatite at a 2 μm scale.

3.2.1.2. XRD analysis. Fig. 2 illustrates the outcomes obtained from XRD analysis to assess the scaffolds content in further detail. In each sample, the predominant phases detected were HA and TCP closely matching the well-defined patterns of these phases as per the ICDD standard cards (JCPDS 09–0432 for HA and JCPDS 009–0169 for TCP) [31]. Distinct diffraction peaks were observed at specific crystal faces of single crystalline HA, namely (002), (211), (112), (300), (202), and (203) [32,33]. The XRD patterns showed that, the peaks associated with SA are notably faint in the XRD patterns, likely due to its lower content compared to HA and TCP, with the broad peaks at 2θ 13°–21° The absence of sharp diffraction peaks suggests that the polymer chains do not arrange themselves into a regular, repeating lattice structure, which is characteristic of crystalline materials [33]. The variation in peaks results from distinct types of HA in different scaffolds. As reported earlier, organic matter in biologically synthesized HA can prevent the emergence of sharper peaks. Both BHA and PHA may be affected by this issue [17,34]. However, BHA had sintered well, and PHA was purified from organic matter and thoroughly mixed into scaffold solutions. Consequently, this process resulted in distinct and clean peaks in the XRD patterns for both PHA and BHA. Sharper peak related to calcite at 2θ value of 39° (JCPDS 5–586) were detected in the XRD pattern of the PHA scaffold. Previous reports have identified peaks corresponding to HA and calcite formed by probiotic bacteria [14]. Calcite, identified as one of the bio-ceramics contributing to osteogenesis, suggests diverse applications in medicine and orthopaedics [14]. These findings indicate that in preparing the composite scaffold, both HA and calcite were effectively integrated into the scaffolds, enhancing the suitability of the

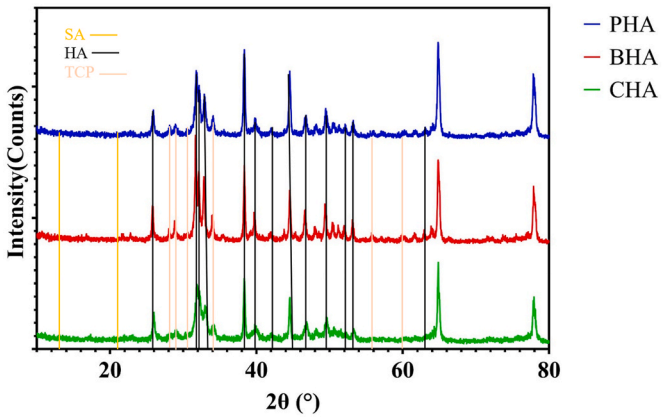

Fig. 2. X-ray diffraction patterns of PHA, BHA, and CHA scaffolds illustrating predominant phases of hydroxyapatite (HA) and tricalcium phosphate (TCP), verified against ICDD standard cards.

PHA scaffold for bone grafting. The XRD findings verified that the crystal structure of HA remained intact in all scaffold types, indicating a thorough and well-mixed incorporation within the scaffold.

3.2.2. Chemical and thermal analysis of the scaffolds

3.2.2.1. FTIR spectroscopy. Fig. 3 illustrates the FTIR findings. In the analysis of CHA, an intense peak at ~1000 cm^{-1}, corresponding to the asymmetric stretching of PO_4^{3-}, was observed, sharper than in PHA and BHA. Additionally, bands at ~1600 cm^{-1} indicated the O-H stretching vibration of liquid water. Phosphate group signals (PO_4^{3-}) were detected at 566 cm^{-1}, 604 cm^{-1}, 962 cm^{-1}, and 1095 cm^{-1}. Weak peaks between ~3200 and 3500 cm^{-1} indicated the stretching of OH group. The presence of carbonate groups (CO_3^{2-}) was confirmed by a signal at 1420 cm^{-1}. Furthermore, the FTIR analysis of BHA and PHA scaffolds exhibited similar spectral patterns to the commercial model, with peaks at 1020 cm^{-1} and 602 cm^{-1} indicating phosphate group presence, confirming the successful incorporation of these two HAs into the scaffold. This underscores the importance of selecting the appropriate HA source in biomaterial design to achieve desired material characteristics. Various characteristic bands were identified, including one at 1644 cm^{-1} representing hydroxyl group bending in absorbed water and the 630 cm^{-1} peak denoting apatite's crystal structure [18,35–37]. The distinct peaks in PHA prompt further investigation into the specific chemical and structural alterations induced by bacterial HA, highlighting the potential for innovative biomaterial designs with tailored properties.

3.2.2.2. DSC analysis. To explore the thermal characteristics of composite scaffolds, DSC was employed within a temperature range spanning from 20 °C to 400 °C. DSC thermograms for PHA, BHA, and CHA are depicted in Fig. 4. The amorphous linear polymer SA lacks a well-defined melting point. The glycosidic bonds in alginate break and create intermediate molecules because the C–O link is less stable at higher temperatures [38]. Pure HA is recognized for having a melting temperature (Tm) surpassing 350° [19].

The peak observed at 80–90 °C is associated with the removal of surface-absorbed water from HA and the melting temperature of SA, influenced by parameters such as agglomerates and the self-assembly of HA particles. As the temperature rises to 400 °C, the peak at 230 °C indicates the removal of crystallization water [19,20]. The PHA composite demonstrated elevated Tm temperatures, suggesting improved thermal stability. This enhancement is attributed to effective interfacial bonding between HA and sodium SA, and the restricted mobility of the SA polymer chain resulting from strong bonding. A single melting peak signifies good miscibility, while multiple melting peaks suggest

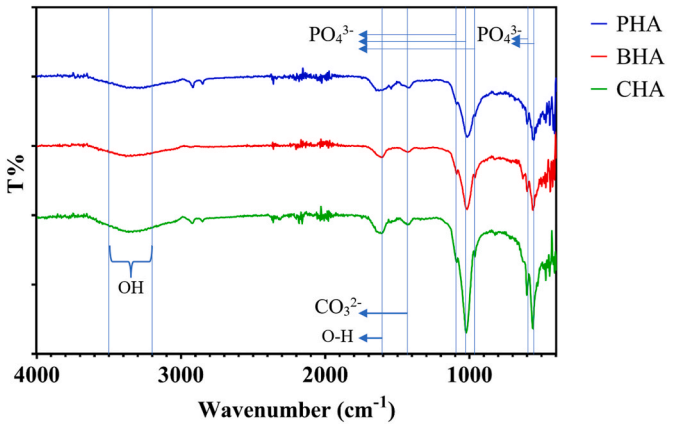

Fig. 3. Comparison of FTIR spectra of probiotic mediated, bovine and commertial hydroxyapatite within the wavenumber range of 4000 to 400 cm^{-1}.

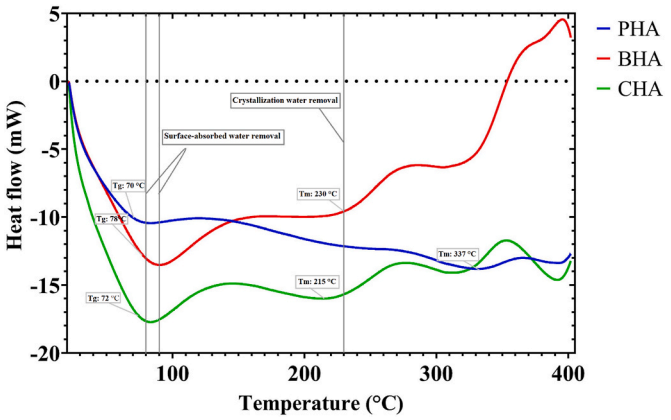

Fig. 4. Differential scanning calorimetry (DSC) thermograms of PHA, BHA, and CHA scaffolds reveal distinct thermal characteristics within a temperature range of 20 °C–400 °C. PHA exhibits elevated melting temperatures (Tm), indicating enhanced thermal stability attributed to effective interfacial bonding between hydroxyapatite (HA) and sodium alginate (SA).

immiscibility, partial miscibility, or the presence of different polymers [19,20,39]. The components were either incompatible or partially incompatible in the blend polymer solution of BHA and CHA. Conversely, in the blend of PHA, the components exhibited compatibility. The primary distinction between HA from probiotics and the other two types lies in their morphology, particle sizes, and the presence of calcite in HA derived from probiotic bacteria. Nano HA acts as a nucleating agent, promoting the formation of more perfect crystallites of polymer in scaffolds and increasing the Tm and thermal stability. Literature confirms that the presence of nanoparticles could lead to modulation of the thermal behavior of the blends [40,41].

3.2.3. Wettability

3.2.3.1. In vitro swelling properties. In investigations related to bone tissue engineering, evaluating the swelling properties of scaffolds is critical as it provides insights into the post-implantation behavior and the effectiveness of absorbing body fluids, wound exudates, and facilitating nutrient transfer within the scaffold [21]. Fig. 5 showed the swelling rates of PHA, CHA, and BHA scaffolds over specified time intervals at a temperature of 37 °C. According to the findings on the swelling behavior of the composite scaffolds, the highest swelling rate

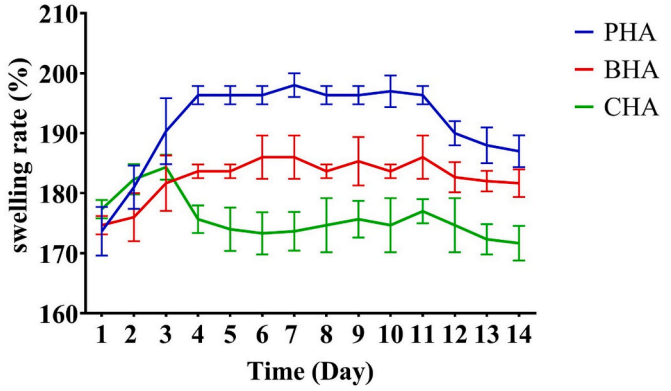

Fig. 5. Swelling Behavior of PHA, CHA, and BHA Scaffolds. Swelling rates (%) of PHA (195 %), CHA (182 %), and BHA (186 %) scaffolds measured over time at 37 °C depict initial high absorption rates with plateauing in PHA and BHA after day 11. The observed behavior suggests osmotic pressure-driven water migration and subsequent degradation, crucial for tissue regeneration and scaffold functionality. Each test was repeated three times.

was observed in the case of PHA (195 %); for BHA and CHA, this ratio was 186 % and 182 %, respectively. All three scaffolds exhibited swelling behavior up to the conclusion of the third day, and the swelling rate in PHA and BHA scaffolds remained plateaued until the 11th day, after which it declined. Figure SI3 illustrated CHA, BHA, and PHA scaffolds before and after 24 h swelling in PBS. The initial increase in the swelling rate in the early stages is attributed to osmotic pressure-driven water migration into the polymeric network. The subsequent decline in the swelling rate post the third day for CHA and the 11th day for PHA and BHA is attributed to the initiation of partial degradation. The swelling characteristics of scaffolds play a pivotal role in the regeneration of damaged tissues, with a higher swelling rate being advantageous for facilitating the transport of nutrients and waste materials. Immersing scaffolds in aqueous media can reduce certain mechanical properties due to swelling, but it also alters pore size, enabling cell adhesion and migration. Subtle water absorption and minor swelling serve to bridge the narrow space between the scaffold and the bone defect. Current findings compare to literature, in turn, ensure cell infiltration into the scaffold, promoting cell adhesion and movement at the interface within the scaffold and the bone tissue [21,42,43].

The swelling response is influenced by the polymer's porosity and hydrophilic properties. SA, known for its pronounced hydrophilicity and porosity, demonstrates high effectiveness in swelling and water absorption. However, after ion cross-linking, the gel exhibits a lower swelling capacity, reduced mobility, and decreased hydrophilicity. Introducing a substantial 40 % w/w of HA to the calcium alginate gel, while weakening the cross-links, enhances the amount of water that permeates the structure and increases swelling. Consequently, the swelling characteristics of the nanocomposite gel can be controlled and improved by adjusting the quantity of the introduced inorganic reinforcement, in this case, HA [44,45].

3.2.3.2. In vitro degradation properties. As shown in Fig. 6, the degradation assessment extended over 15 days, indicating that the degradation behavior of PHA, BHA, and CHA scaffolds is quite similar. The degradation rate of the CHA scaffold group was the fastest, reaching a degradation rate of 60 % on day 15. In contrast, the degradation rates of the PHA and BHA scaffold groups were relatively stable, at 37 % and 44 %, respectively, on day 15. The optimal scenario is for the scaffold's disintegration rate at the bone defect to align with the rate at which new bone is growing. Since these characteristics exhibit a linear relationship with the total crosslinking density, scaffold mechanical stiffness is often directly proportional to the scaffold breakdown rate [46]. The optimal period of this reaction was aligned with provided data. The pace of bone tissue regeneration is considerably slower than that of soft tissue regeneration. Hence, if the scaffold degrades too quickly during the early stages of bone formation, it may not adequately support the bone tissue regeneration process [42]. Consequently, this could result in the intrusion of soft tissue into the bone defect, which is unfavorable for the regeneration of bone structure. Research indicates that materials with higher water absorption and superior swelling properties tend to experience more rapid weight loss [21]. In this case, the micro/nanostructure and morphology of the materials can influence how water interacts with them and how degradation proceeds. A higher surface area-to-volume ratio may significantly increase the solubility of the construct and render it more resorbable. Even though PHA may absorb more water and swell more, its nanostructure or braided morphology could hinder the degradation process compared to BHA and CHA with microsize and granular shape [47].

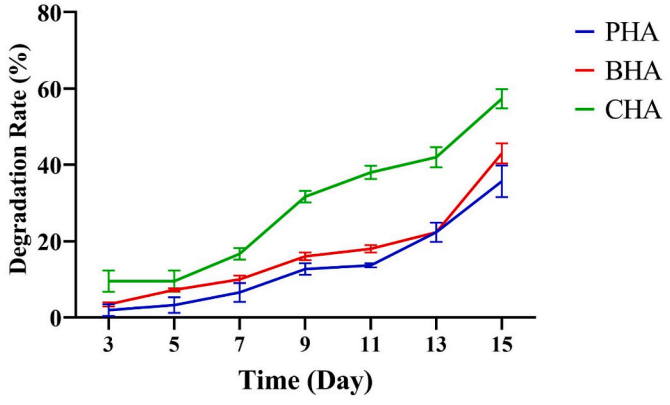

Fig. 6. Comparison of degradation rates (%) for PHA, BHA, and CHA scaffolds during a 15-day incubation period. CHA scaffolds exhibited the highest degradation rate, reaching 60 %, while PHA and BHA scaffolds showed more stable degradation rates of 37 % and 44 %, respectively. Each test was repeated three times.

3.2.4. Mechanical properties

The mechanical properties of scaffolds should closely mimic those of the bone tissue being replaced. For example, scaffolds with higher stiffness may cause stress shielding, while lower stiffness levels may lead to insufficient mechanical stability for the lesion [22]. This study specifically examined the compressive strength of scaffolds constructed from PHA, CHA, and BHA (Table 1). The results indicate that scaffolds incorporating probiotic bacterial HA (PHA) exhibit a superior compressive strength of 10 ± 0.02 MPa compared to CHA (6.91 ± 1.44 MPa) and BHA (6.72 ± 1.68 MPa). When analysing the strain values (%) of the constructs, it became evident that the PHA scaffold displayed the highest strain at 29.26 ± 4.63 %. In contrast, the BHA scaffold exhibited the lowest strain at 19.24 ± 8.95 %. A decrease in strain values contributes to an increase in the brittleness of the material. Upon a thorough assessment of both compressive strengths and strain values, it is evident that the PHA scaffold displays superior mechanical properties. This superiority is attributed to its remarkable ability for substantial deformation and effective force absorption before fracture [23]. The results of the compression test conducted in this investigation revealed that the compressive strength values of the manufactured scaffolds indicate the suitability of PHA for applications in bone tissue, given its favorable mechanical properties. The compressive strength exhibited by the scaffolds in this study demonstrates notable competitiveness compared to existing literature, which reported that the compressive strength of trabecular bone is in the range of 0.1–16 MPa, thus highlighting the significance of our findings in the development of scaffolds for biomedical applications [22,24]. Incorporating bacterial HA which has nano size into materials showed a notable enhancement in compression test results, primarily attributed to its nanoscale properties and the resulting superior reinforcing surface-to-volume ratio of nano HA. Research indicates that the increased surface area of nano-HA when compared to micro sized HA, facilitates stronger bonding between the nano-sized HA particles and the polymer. This enhanced bonding leads to greater reinforcement of the polymer matrix, ultimately improving the mechanical and functional characteristics of nanocomposites in contrast to conventional micro-composites. This phenomenon likely elucidates why scaffolds containing nano-HA exhibit greater consistency in size and morphology. The nano-sized particles are more effectively distributed within the polymer matrix and securely bound to it, resulting

Table 1
Compression testing results for PHA, BHA, and CHA scaffolds. PHA had significant difference $p < 0.0001$ = **** with BHA and CHA in compressive strength, as well as $p < 0.0001$ = **** with BHA and $p < 0.01$ = ** with CHA in strain. Each test was repeated three times.

Scaffolds	Strain (%)	Compressive Strength (MPa)
PHA	29.26 ± 4.63	10 ± 0.02
BHA	19.24 ± 8.95	6.72 ± 1.68
CHA	23.46 ± 13.07	6.912 ± 1.44

in a more uniform and reinforced structure. This remarkable strength can be attributed mainly to the unique shape and nano-sized nature of the reported bacterial HA [14,48–50].

3.3. Cell culture analysis

3.3.1. MTT assay

The cell proliferation rate was evaluated using the tetrazolium salt MTT. As shown in Fig. 7(A), the 3D-printed PHA scaffolds displayed higher absorbance values than the BHA and CHA scaffolds over the entire 21 days of cultivation. Cell viability is closely associated with the extent of reduction, measurable through a spectrophotometer. As depicted in Fig. 7, the lowest cell viability was observed for TCPS and CHA. In contrast, the most substantial cell viability was noted in PHA scaffolds, followed by BHA scaffolds, after the 21-day cultivation period. Current research carried out with MC3T3-E1 cell cultures has presented compelling evidence in favor of the efficacy of probiotic bacterial HA. The findings reveal that when scaffolds containing probiotic bacterial HA were introduced to MC3T3-E1 cells, their proliferation increased significantly by 174 %. This notable increase, more than observed in the control group, likely indicates a shift toward osteoblast commitment. Subsequently, complementary investigations, such as ALP and alizarin red staining, were conducted to validate this hypothesis. The findings align with prior research, suggesting that probiotic bacterial HA not only lacked a toxic effect but also enhanced the proliferation of stem cells and their differentiation into osteoblastic cells [21]. In previous findings by the authors, probiotics with synthesized HA significantly stimulated stem cell proliferation compared to probiotics without HA, indicating the positive impact of bacteria-synthesized HA on cell multiplication. Nano-HA acts as a catalyst for bone formation by promoting the differentiation and activity of osteoblasts, providing essential calcium and phosphate near stem cells, thus aiding bone regeneration. The small crystal size of nano-HA creates higher stress levels at the cell-crystal interface compared to micro-HA, enhancing cell extension on its surface and facilitating calcium ion exchange. This promotes the differentiation of stem cells into osteoblasts. Additionally, nano-HA aids in the attachment of specific cells dependent on surface adhesion by adsorbing extracellular matrix proteins like fibronectin and growth factors such as osteonectin [15].

3.3.2. ALP activity

The outcomes from the spectrophotometric assessment of ALP activity in MC3T3-E1 cells grown on PHA, BHA, and CHA scaffolds throughout 7, 14, and 21 days are displayed in Fig. 7(B). As depicted, ALP activity has an upward trend as the incubation period extends. This discovery suggests that the cells effectively performed osteogenic functions on the scaffolds [27,28]. The elevated ALP activity observed in the PHA scaffolds (15.3 U/mg), compared to the BHA and CHA scaffolds, signifies the superior capability of scaffolds containing probiotic bacterial HA to foster cell differentiation. It has been previously shown that HA synthesized from the probiotic bacteria *Bacillus coagulase* can differentiate stem cells into bone cells [15]. ALP stands out as a widely acknowledged biochemical marker indicating the activity of bone progenitor cells and is thought to contribute to bone mineralization. Scaffolds intended for applications in bone tissue engineering must facilitate the differentiation of bone progenitor cells into functional bone tissue [25,27,28].

3.3.3. Alizarin red staining

Alizarin Red Staining was performed on the 7th, 14th, and 21st days of cultivation to identify extracellular calcium deposition on TCPS, PHA, BHA, and CHA throughout the cultivation period. Mineralization from

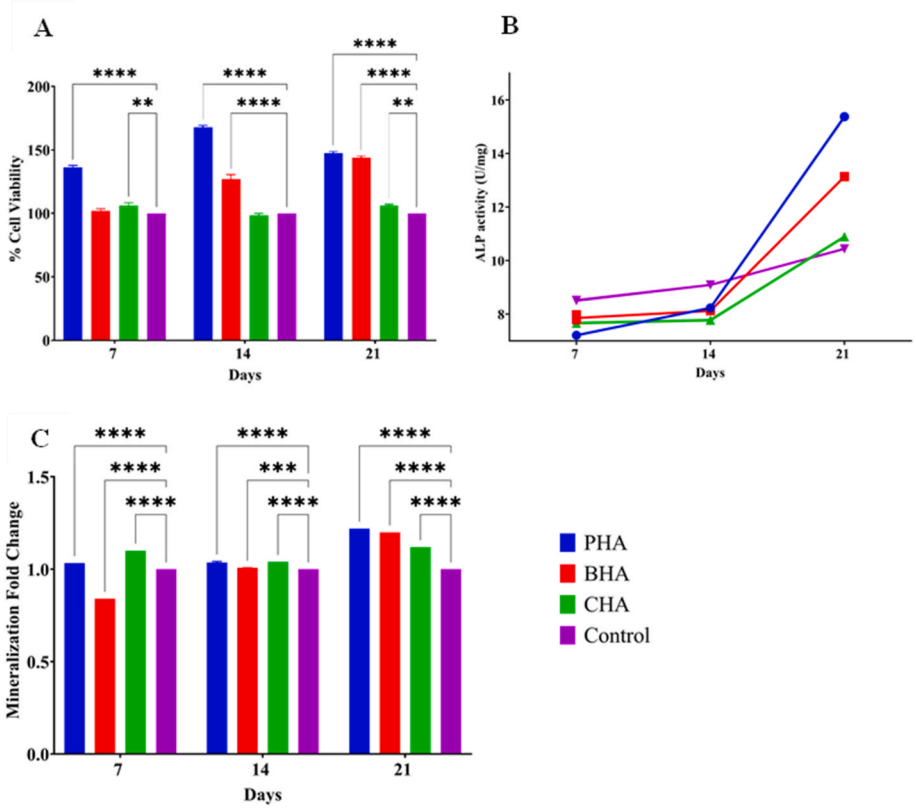

Fig. 7. Absorbance values of MC3T3-E1 cell viability obtained with the MTT assay (A); alkaline phosphatase activity (B); and quantitative mineralization assessment, conducted by measuring the absorbance of the extracted alizarin red dye (C) on the 3D-printed scaffolds. Results are presented as Mean ± SD; n = 3. All sets of data exhibit significant differences (*p < 0.05), Statistical significance 'p' is represented as, p < 0.05 = '*', p < 0.01 = '**', p < 0.001 = '***', p < 0.0001 = '****'. Each test was repeated three times. (For interpretation of the references to colour in this figure legend, the reader is referred to the Web version of this article.)

the scaffolds was quantified by measuring the dye removed from the stained nodules using spectrophotometry. Fig. 7(C) displays the absorbance measurements for alizarin red S collected from nodules and cells on the scaffolds and control wells. The higher absorbance values observed in the cell lysates obtained from the PHA and BHA scaffolds indicate that these scaffolds have a greater potential to support mineralization. In addition to the preliminary assessment of ALP activity, serving as a marker for the unique role of MC3T3-E1 cells, alizarin red-positive nodules are indicative of mineralization, a late event in the process of bone development [27,28]. A crucial aspect in developing scaffolds for bone tissue engineering involves evaluating the production of mineralized matrix and nodules by bone progenitor cells [25]. The PHA scaffolds demonstrated a superior capacity (1.22-fold) to facilitate mineralization by MC3T3-E1 cells compared to both the BHA and CHA scaffolds at various assay times and in comparison to the control wells. This suggests an enhanced cellular response in scaffolds containing probiotic bacterial HA.

4. Conclusion

The synthesis of probiotic bacterial HA powder was accomplished, and compared to commercial and bovine types of HA. Utilizing 3D printing technology, we successfully manufactured scaffolds for bone tissue engineering, incorporating composite materials of PHA, BHA, and CHA. To bolster the mechanical strength of the produced composite scaffolds and impede their degradation, crosslinking was carried out using $CaCl_2$. The addition of bacterial HA to the SA and TCP solution increased viscosity. Upon scrutinizing the SEM images of the resulting scaffolds, it was evident that the PHA scaffold was excellently formed with a pore size of 472.17 $\pm$ 18.51 μm. This size aligns with recommendations in the literature for promoting cellular growth and bone ingrowth in bone tissue engineering. XRD, FTIR, and DSC findings revealed a robust interaction among the components, indicating superior thermal stability for PHA compared to BHA and CHA. The inclusion of probiotic bacterial HA led to higher compressive strength and strain values for PHA composite scaffolds, demonstrating resistance when swelling and degradation compared to other composite types. Biocompatibility tests emphasized the significant role of scaffolds, especially those incorporating probiotic bacterial HA, in facilitating optimal cell proliferation, differentiation, and mineralization. The findings of this research highlight the promising potential of PHA 3D composite scaffolds for advancing bone implants in biomedical applications and pave the way for more sophisticated and effective 3D printed scaffold designs, utilizing novel, naturally derived, and safely synthesized biomaterials. The production of probiotic bacterial hydroxyapatite is currently not affordable. However, its texture and associated feature demonstrate that it offers superior characteristics compared to other types, providing better qualities to the hydroxyapatite scaffold. Given its potential to improve the structure in 3D bone printing, it is essential to study its structure in detail to understand the reasons behind these beneficial formations.

Ethical statement

The authors declare that there are no conflicts of interest.

CRediT authorship contribution statement

Sabereh Nouri: Writing – original draft, Visualization, Software, Methodology, Investigation, Formal analysis, Data curation, Conceptualization. **Giti Emtiazi:** Writing – review & editing, Validation, Resources, Project administration, Methodology, Conceptualization. **Songul Ulag:** Writing – review & editing, Validation, Supervision, Project administration. **Oguzhan Gunduz:** Writing – review & editing, Validation, Supervision, Project administration, Funding acquisition. **Ayse Ceren Calikoglu Koyuncu:** Writing – review & editing, Methodology. **Rasoul Roghanian:** Writing – review & editing, Supervision, Project administration. **Armaghan Moradi:** Writing – review & editing. **Rasoul Shafiei:** Writing – review & editing, Validation, Conceptualization. **Ari Tukay:** Writing – review & editing, Methodology. **Hilal Turkoglu Sasmazel:** Writing – review & editing, Methodology.

Declaration of competing interest

The authors declare that they have no known competing financial interests or personal relationships that could have appeared to influence the work reported in this paper.

Data availability

Data will be made available on request.

Acknowledgment

The authors thank the Microbiology Lab at the University of Isfahan, Iran, the Center for Nanotechnology & Biomaterials Application and Research (NBUAM) at Marmara University, Istanbul, Turkey, and the Metallurgical and Materials Engineering Department, Faculty of Engineering, Atilim University, Incek, Ankara, Turkey.

Appendix A. Supplementary data

Supplementary data to this article can be found online at https://doi.org/10.1016/j.polymer.2024.127523.

References

[1] S. Nouri, R. Roghanian, G. Emtiazi, Review on biological synthesis of nano-hydroxyapatite and its application in nano-medicine, Iran. J. Microbiol. 15 (2021) 369–383, https://doi.org/10.30699/ijmm.15.4.369.
[2] N. Amiryaghoubi, M. Fathi, N.N. Pesyan, M. Samiei, J. Barar, Y. Omidi, Bioactive polymeric scaffolds for osteogenic repair and bone regenerative medicine, Med. Res. Rev. 40 (2020) 1833–1870, https://doi.org/10.1002/med.21672.
[3] A. Iglesias-Mejuto, C.A. García-González, 3D-printed alginate-hydroxyapatite aerogel scaffolds for bone tissue engineering, Mater. Sci. Eng. C 131 (2021) 112525, https://doi.org/10.1016/j.msec.2021.112525.
[4] H. Sun, C. Hu, C. Zhou, L. Wu, J. Sun, X. Zhou, et al., 3D printing of calcium phosphate scaffolds with controlled release of antibacterial functions for jaw bone repair, Mater. Des. 189 (2020) 108540, https://doi.org/10.1016/j.matdes.2020.108540.
[5] S. Bose, S. Vahabzadeh, A. Bandyopadhyay, Bone tissue engineering using 3D printing, Mater. Today 16 (2013) 496–504, https://doi.org/10.1016/j.mattod.2013.11.017.
[6] F. Hao, S. Sun, Y. Xu, X. Maimaitiyiming, 3D printing of flexible sensors based on polyvinyl alcohol/carboxylated chitosan/sodium alginate/silver nanowire high-strength hydrogels, Polymer 290 (2024) 126594, https://doi.org/10.1016/j.polymer.2023.126594.
[7] K.K. Dey, S. Gayen, M. Ghosh, Structure and dynamics of sodium alginate as elucidated by chemical shift anisotropy and site-specific spin–lattice relaxation time measurements, Eur. Biophys. J. 50 (2021) 963–977, https://doi.org/10.1007/s00249-021-01559-9.
[8] Z. Liu, X. He, S. Chen, H. Yu, Advances in the use of calcium silicate-based materials in bone tissue engineering, Ceram. Int. 49 (2023) 19355–19363, https://doi.org/10.1016/j.ceramint.2023.03.063.
[9] M. Sadat-Shojai, M.-T. Khorasani, E. Dinpanah-Khoshdargi, A. Jamshidi, Synthesis methods for nanosized hydroxyapatite with diverse structures, Acta Biomater. 9 (2013) 7591–7621, https://doi.org/10.1016/j.actbio.2013.04.012.
[10] V. DileepKumar, M.S. Sridhar, P. Aramwit, V.K. Krut'ko, O.N. Musskaya, I. E. Glazov, et al., A review on the synthesis and properties of hydroxyapatite for biomedical applications, J. Biomater. Sci. Polym. Ed. 33 (2022) 229–261, https://doi.org/10.1080/09205063.2021.1980985.
[11] B. Pemmer, A. Roschger, A. Wastl, J. Hofstaetter, P. Wobrauschek, R. Simon, et al., Spatial distribution of the trace elements zinc, strontium and lead in human bone tissue, Bone 57 (2013) 184–193, https://doi.org/10.1016/j.bone.2013.07.038.
[12] R.G. Saratale, I. Karuppusamy, G.D. Saratale, A. Pugazhendhi, G. Kumar, Y. Park, et al., A comprehensive review on green nanomaterials using biological systems: recent perception and their future applications, Colloids Surf. B Biointerfaces 170 (2018) 20–35, https://doi.org/10.1016/j.colsurfb.2018.05.045.
[13] A.C. Thackray, R.L. Sammons, L.E. Macaskie, P. Yong, H. Lugg, P.M. Marquis, Bacterial biosynthesis of a calcium phosphate bone-substitute material, J. Mater.

Sci. Mater. Med. 15 (2004) 403–406, https://doi.org/10.1023/B:JMSM.0000021110.07796.6e.
[14] S. Nouri, R. Roghanian, G. Emtiazi, R. Shafiei, Biosynthesis of nano-calcite and nano-hydroxyapatite by the probiotic bacteria of Bacillus subtilis and Bacillus coagulans, Appl Food Biotechnol 9 (2022) 275–286, https://doi.org/10.22037/afb.v9i4.38768.
[15] S. Nouri, R. Roghanian, G. Emtiazi, O. Gunduz, R. Shafiei, Osteoblastic differentiation of stem cells from human exfoliated deciduous teeth by probiotic hydroxyapatite, Cell J 25 (2023) 753, https://doi.org/10.22074/CELLJ.2023.1999743.1276.
[16] A. R Naqshbandi, I. Sopyan, Development of porous calcium phosphate bioceramics for bone implant applications: a review, Recent Pat. Mater. Sci. 6 (2013) 238–252.
[17] Y. Moukbil, B. Isindag, V. Gayir, B. Ozbek, M.E. Haskoylu, E.T. Oner, et al., 3D printed bioactive composite scaffolds for bone tissue engineering, Bioprinting 17 (2020) e00064, https://doi.org/10.1016/j.bprint.2019.e00064.
[18] S. Iswarya, T. Theivasanthi, K. Chinnaiah, S.C. Gopinath, Sodium alginate/hydroxyapatite/graphene nanoplatelets composites for bone tissue engineering, Appl. Nanosci. 14 (2024) 109–122, https://doi.org/10.1007/s13204-023-02967-3.
[19] Y. Song, K. Joo, J.H. Seo, Evaluation of mechanical and thermal properties of hydroxyapatite-levan composite bone graft, Biotechnol. Bioproc. Eng. 26 (2021) 201–207, https://doi.org/10.1007/s12257-020-0094-6.
[20] K.M. Tohamy, M. Mabrouk, I.E. Soliman, H.H. Beherei, M.A. Aboelnasr, Novel alginate/hydroxyethyl cellulose/hydroxyapatite composite scaffold for bone regeneration: in vitro cell viability and proliferation of human mesenchymal stem cells, Int. J. Biol. Macromol. 112 (2018) 448–460, https://doi.org/10.1016/j.ijbiomac.2018.01.181.
[21] E. Saylam, Y. Akkaya, E. Ilhan, S. Cesur, E. Guler, A. Sahin, et al., Levodopa-loaded 3D-printed poly (lactic) acid/chitosan neural tissue scaffold as a promising drug delivery system for the treatment of Parkinson's disease, Appl. Sci. 11 (2021) 10727, https://doi.org/10.3390/app112210727.
[22] L.-C. Gerhardt, A.R. Boccaccini, Bioactive glass and glass-ceramic scaffolds for bone tissue engineering, Materials 3 (2010) 3867–3910, https://doi.org/10.3390/ma3073867.
[23] Q. Wei, D. Sun, M. Li, J. Zhou, R. Yang, J. Zhang, et al., Modification of hydroxyapatite (HA) powder by carboxymethyl chitosan (CMCS) for 3D printing bioceramic bone scaffolds, Ceram. Int. 49 (2023) 538–547, https://doi.org/10.1016/j.ceramint.2022.09.021.
[24] E. Ryan, S. Yin, Compressive strength of β-TCP scaffolds fabricated via lithography-based manufacturing for bone tissue engineering, Ceram. Int. 48 (2022) 15516–15524, https://doi.org/10.1016/j.ceramint.2022.02.085.
[25] A. Hassani, Ç.B. Avci, S.N. Kerdar, H. Amini, M. Amini, M. Ahmadi, et al., Interaction of alginate with nano-hydroxyapatite-collagen using strontium provides suitable osteogenic platform, J. Nanobiotechnol. 20 (2022) 310, https://doi.org/10.1186/s12951-022-01511-9.
[26] A.O. Basar, V. Sadhu, H.T. Sasmazel, Preparation of electrospun PCL-based scaffolds by mono/multi-functionalized GO, Biomed. Mater. 14 (2019) 045012, https://doi.org/10.1088/1748-605X/ab2035.
[27] S.A. Mosaddad, M. Yazdanian, H. Tebyanian, E. Tahmasebi, A. Yazdanian, A. Seifalian, et al., Fabrication and properties of developed collagen/strontium-doped Bioglass scaffolds for bone tissue engineering, J. Mater. Res. Technol. 9 (2020) 14799–14817, https://doi.org/10.1016/j.jmrt.2020.10.065.
[28] Q. Fu, M.N. Rahaman, B.S. Bal, R.F. Brown, In vitro cellular response to hydroxyapatite scaffolds with oriented pore architectures, Mater. Sci. Eng. C 29 (2009) 2147–2153, https://doi.org/10.1016/j.msec.2009.04.016.
[29] M.O. Aydogdu, B. Mutlu, M. Kurt, A.T. Inan, S.E. Kuruca, G. Erdemir, et al., Developments of 3D polycaprolactone/beta-tricalcium phosphate/collagen scaffolds for hard tissue engineering, Journal of the Australian Ceramic Society 55 (2019) 849–855, https://doi.org/10.1007/s41779-018-00299-y.
[30] S. Sonika, H.E. Nalini, R.R. Devi, Quintessential commence of three-dimensional printing in periodontal regeneration-A review, Saudi Dent J 35 (2023) 876–882, https://doi.org/10.1016/j.sdentj.2023.07.002.
[31] X. Liu, Y. Zhang, K. Xiong, M. Yan, Fabrication of a novel beta tricalcium phosphate/sodium alginate/poly (D, L-lactic acid) composite microsphere and its drug releasing property, J. Nanosci. Nanotechnol. 18 (2018) 3844–3849, https://doi.org/10.1166/jnn.2018.15026.
[32] T. Huang, C. Fan, M. Zhu, Y. Zhu, W. Zhang, L. Li, 3D-printed scaffolds of biomineralized hydroxyapatite nanocomposite on silk fibroin for improving bone regeneration, Appl. Surf. Sci. 467 (2019) 345–353, https://doi.org/10.1016/j.apsusc.2018.10.166.
[33] H. Luo, G. Zuo, G. Xiong, C. Li, C. Wu, Y. Wan, Porous nanoplate-like hydroxyapatite–sodium alginate nanocomposite scaffolds for potential bone tissue engineering, Mater. Technol. 32 (2017) 78–84, https://doi.org/10.1080/10667857.2015.1125045.
[34] S. Pramanik, A.S.M. Hanif, B. Pingguan-Murphy, N.A. Abu Osman, Morphological change of heat treated bovine bone: a comparative study, Materials 6 (2012) 65–75, https://doi.org/10.3390/ma6010065.
[35] S. Koutsopoulos, Synthesis and characterization of hydroxyapatite crystals: a review study on the analytical methods, J. Biomed. Mater. Res. 62 (2002) 600–612, https://doi.org/10.1002/jbm.10280.
[36] C. Onoyima, F. Okibe, E. Agbaji, V. Ajibola, Preparation, characterization and in-vitro drug release study of methotrexate-loaded hydroxyapatite-sodium alginate nanocomposite, International Journal Of Science for Global Sustainability 2 (2016) 12. https://fugus-ijsgs.com.ng/index.php/ijsgs/article/view/245.
[37] J. Ghilotti, I. Fernández, J.L. Sanz, M. Melo, C. Llena, Remineralization potential of three restorative glass ionomer cements: an in vitro study, J. Clin. Med. 12 (2023) 2434, https://doi.org/10.3390/jcm12062434.
[38] L. Iskandar, L. Rojo, L. Di Silvio, S. Deb, The effect of chelation of sodium alginate with osteogenic ions, calcium, zinc, and strontium, J. Biomater. Appl. 34 (2019) 573–584, https://doi.org/10.1177/0885328219861904.
[39] Investigation on high-temperature decomposition characteristic of hydroxyapatite, in: C. Wang, R. Quan, H. Wang, X. Wei, Z. Zhao (Eds.), 2009 IEEE 3rd International Conference on Nano/Molecular Medicine and Engineering, IEEE, 2009.
[40] S. Bonardd, M. Schmidt, M. Saavedra-Torres, A. Leiva, D. Radic, C. Saldías, Thermal and morphological behavior of chitosan/PEO blends containing gold nanoparticles. Experimental and theoretical studies, Carbohydr. Polym. 144 (2016) 315–329, https://doi.org/10.1016/j.carbpol.2016.02.071.
[41] F.M. Ghorbani, B. Kaffashi, P. Shokrollahi, S. Akhlaghi, M.S. Hedenqvist, Effect of hydroxyapatite nano-particles on morphology, rheology and thermal behavior of poly (caprolactone)/chitosan blends, Mater. Sci. Eng. C 59 (2016) 980–989, https://doi.org/10.2174/1874464811306990012.
[42] D. Liu, Z. Liu, J. Zou, L. Li, X. Sui, B. Wang, et al., Synthesis and characterization of a hydroxyapatite-sodium alginate-chitosan scaffold for bone regeneration, Front Mater 8 (2021) 648980, https://doi.org/10.3389/fmats.2021.648980.
[43] K. Aranci, M. Uzun, S. Su, S. Cesur, S. Ulag, A. Amin, et al., 3D propolis-sodium alginate scaffolds: influence on structural parameters, release mechanisms, cell cytotoxicity and antibacterial activity, Molecules 25 (2020) 5082, https://doi.org/10.3390/molecules25215082.
[44] B.C. Alves, RdS. Miranda, B.M. Frigieri, D.A. Zuccari, MRd Moura, F.A. Aouada, et al., A 3D printing scaffold using alginate/hydroxyapatite for application in bone regeneration, Mater. Res. 26 (2023) e20230051, https://doi.org/10.1590/1980-5373-MR-2023-0051.
[45] M. Mohammadpour, H. Samadian, N. Moradi, Z. Izadi, M. Eftekhari, M. Hamidi, et al., Fabrication and characterization of nanocomposite hydrogel based on alginate/nano-hydroxyapatite loaded with linum usitatissimum extract as a bone tissue engineering scaffold, Mar. Drugs 20 (2021) 20, https://doi.org/10.3390/md20010020.
[46] M. Milojević, G. Harih, B. Vihar, J. Vajda, L. Gradišnik, T. Zidarič, et al., Hybrid 3D printing of advanced hydrogel-based wound dressings with tailorable properties, Pharmaceutics 13 (2021) 564, https://doi.org/10.3390/pharmaceutics13040564.
[47] S. Salmasi, L. Nayyer, A.M. Seifalian, G.W. Blunn, Suppl-3, M8: nanohydroxyapatite effect on the degradation, osteoconduction and mechanical properties of polymeric bone tissue engineered scaffolds, Open Orthop. J. 10 (2016) 900, https://doi.org/10.2174/1874325001610010900.
[48] H.-Y. Mi, X. Jing, M.R. Salick, T.M. Cordie, X.-F. Peng, L.-S. Turng, Morphology, mechanical properties, and mineralization of rigid thermoplastic polyurethane/hydroxyapatite scaffolds for bone tissue applications: effects of fabrication approaches and hydroxyapatite size, J. Mater. Sci. 49 (2014) 2324–2337, https://doi.org/10.1007/s10853-013-7931-3.
[49] H. Liang, Y. Wang, S. Chen, Y. Liu, Z. Liu, J. Bai, Nano-hydroxyapatite bone scaffolds with different porous structures processed by digital light processing 3D printing, Int J Bioprint 8 (2022), https://doi.org/10.18063/ijb.v8i1.502.
[50] G. Tetteh, A. Khan, R. Delaine-Smith, G. Reilly, I. Rehman, Electrospun polyurethane/hydroxyapatite bioactive Scaffolds for bone tissue engineering: the role of solvent and hydroxyapatite particles, J. Mech. Behav. Biomed. Mater. 39 (2014) 95–110, https://doi.org/10.1016/j.jmbbm.2014.06.019.